Jinst

Published by IOP Publishing for Sissa Medialab

Received: *September 18, 2019*
Revised: *November 18, 2019*
Accepted: *November 29, 2019*
Published: *January 9, 2020*

Element discrimination via spectroscopic X-ray imaging with a CdTe Medipix3RX detector

M. Schütz,[1] **S. Procz, J. Fey and M. Fiederle**

FMF — Freiburg Material Research Center, University of Freiburg, Stefan-Meier-Straße 21, Freiburg im Breisgau, 79104 Germany

E-mail: michael.schuetz@fmf.uni-freiburg.de

Abstract: X-ray imaging techniques that distinguish radiation in different energy ranges offer the advantage of material differentiation based on the material-specific properties of the object to be examined. One possibility to obtain spectroscopic information is the K-edge approach utilizing energy thresholds. A basic information about the photon energy is needed for this purpose. The Medipix3RX is a photon-counting semiconductor detector which provides multiple energy thresholds in a single recording and so an energy information. It offers up to eight independent energy thresholds per pixel with high spatial and high energy resolution. In order to investigate the possibility of material discrimination by X-ray imaging methods with Medipix3RX detectors, an absorption phantom was fabricated and examined which consists of 8 different materials in various thicknesses. For material separation the K-edge method was used, which exploits the abrupt rise of photo absorption for energies above the ionization energy of electrons in the atomic K-shell. After performing a threshold equalization and a threshold-energy calibration of the detector, X-ray images were taken of the phantom. After evaluation, five of the eight materials of the phantom were successfully separated and identified with the selected settings of the X-ray tube. These include gadolinium and iodine, which are used as contrast agents in oncology. The most reliable material discrimination was achieved for tungsten and gadolinium. Due to their high K-edge energy, they had the greatest influence on the spectrum used. Elements with a low atomic number, however, could be distinguished less confidently due to the low photo absorption in the energy spectrum used and the resulting low effect on the change of the measured total intensity. This article describes the experimental setup of the energy calibration and X-ray image analysis of a Medipix3RX detector with a 1 mm CdTe sensor as well as the performance and evaluation of these and shows first results in material identification with eight energy thresholds in spectroscopic single pixel mode configuration.

Keywords: Hybrid detectors; Imaging spectroscopy; X-ray detectors

[1]Corresponding author.

https://doi.org/10.1088/1748-0221/15/01/P01006

2020 JINST 15 P01006

Contents

2020 JINST 15 P01006

1 Introduction

Since the discovery of X-ray radiation by Wilhelm Conrad Roentgen in 1895, the detection of X-rays has evolved into one of the most important diagnostic tools for non-destructive investigations. Nowadays it is a common tool for medical applications as well as for material researchers, homeland security and industrial purposes. The principle of X-ray detection has changed over the last years from photographic plates to indirect detection via scintillators to direct photo detection with single photon counting, semiconductor detector devices with high energy resolution and high spatial resolution. Along with new detector types, new possibilities for X-ray-based applications occurred. The detector device used in this work, the Medipix3RX detector (MPX3RX), provides the possibility to distinguish between different levels of energy with up to eight independent energy thresholds [1]. This opens new possibilities for X-ray imaging; the differentiation between different energy ranges and, therefore, spectroscopic X-ray imaging. This technology promises advantages in different fields of interest like medicine, Homeland Security, the mining industry and for material science in non-destructive material research. In this work the MPX3RX detector is used to discriminate different materials utilizing the increase of absorption of photons above the ionization energies. The aim of this work was the separation of various materials via the K-edge method with a single energy-selective X-ray acquisition.

2 Materials and methods

2.1 K-edge method

The attenuation of X-rays by an absorber material is a composition of different interaction processes and can be described by Beer-Lambert law. The attenuation is depending on the absorbing material

and the energy of the transmitted photon. Besides coherent and incoherent scattering of photons the photo-absorption by ionization leads to an increase of attenuation. For X-ray photon energies above the electron ionization energy of the specific element the absorption of photons increases drastically. This distinct rise of absorption is visible in the transmission spectrum as a sharp edge as shown in figure 1. The edge in the measured transmission spectrum is called K-edge, L-edge and so on, depending on the corresponding atomic shell. These element specific absorption edges can be used to identify the underlying material. A material identification or separation respectively, related on the ionization of an electron from the K-shell of an atom is called K-edge method.

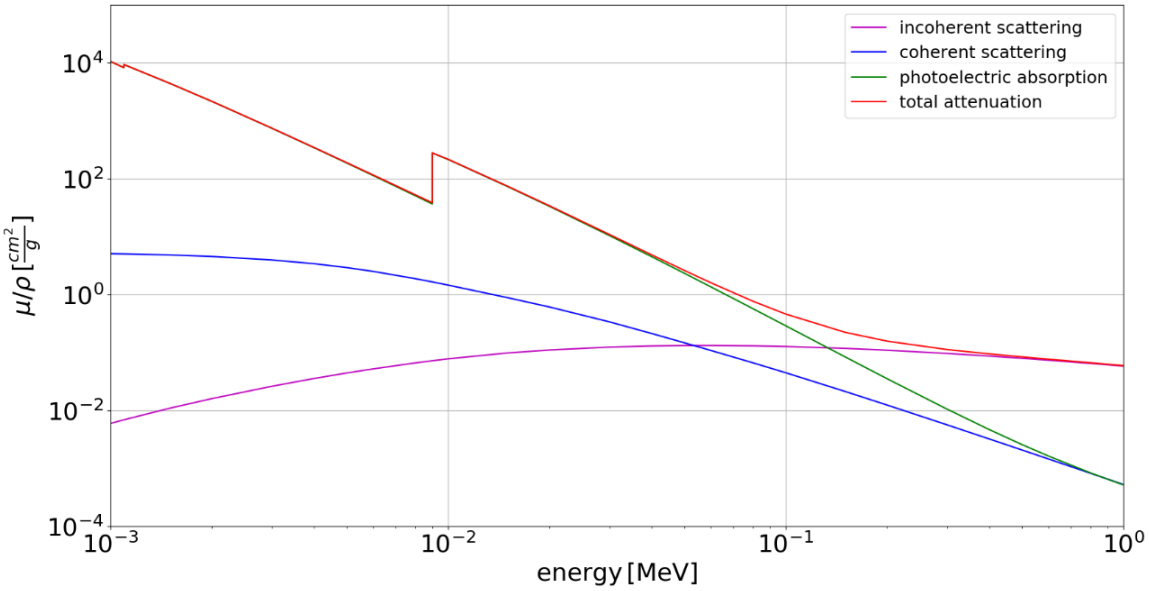

Figure 1. Composition of total photon attenuation in copper by interaction processes. Data from [2].

2.2 Medipix3RX detector

The Medipix3RX detector is a pixelated, hybrid photon counting semiconductor detector device with high spatial resolution and high energy resolution developed by the Medipix3 collaboration at CERN [4]. It has an active area of 1.98 cm^2 and 256×256 pixels with a pixel pitch of 55 µm. Every single pixel has two independent energy thresholds. The Medipix3RX, offers the possibility of two different modes of operation, fine pitch mode and spectroscopic mode which differs in hardware configuration of the readout-chip to sensor connection. In fine pitch mode every pixel of the readout chip is hardware-sided connected to the sensor material providing two energy thresholds per pixel with a pixel pitch of 55 µm. In spectroscopic mode only one of four pixels of the readout chip is bonded to the sensor material while the other three unbonded pixels provide their pixel electronics as additional energy thresholds with independent counters to the bonded pixel. Together, the single bonded and the three unbonded pixels form a super-pixel with eight energy thresholds and a pixel pitch of $110 \times 110\,\mu m^2$. Therefore, every super pixel has a total of eight independent energy thresholds with simultaneous bisection in spatial resolution [1]. The sensor used in this work was a cadmium telluride (CdTe) sensor with 1 mm thickness. CdTe has for the required photon energies,

2020 JINST 15 P01006

from 10 keV to 90 keV, the highest absorption efficiency compared to Silicon or gallium arsenide (GaAs) detectors with the same thicknesses as shown in figure 2.

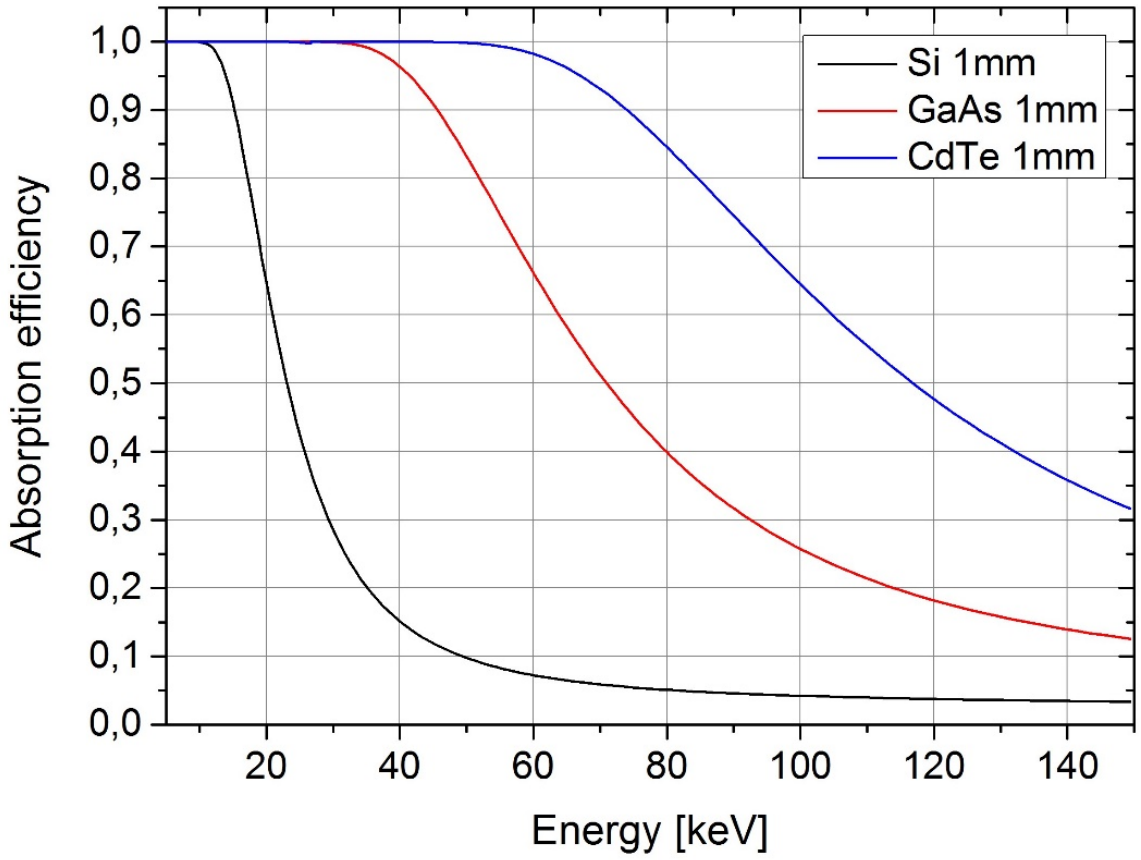

Figure 2. Absorption efficiency for semiconductor materials Si, GaAs, and CdTe for 1 mm sensor thicknesses. Data from [3].

2.3 Absorption phantom

To investigate the possibility of material discrimination via energy selective X-ray imaging, an absorption phantom was developed and produced, covering several fields of interest. The phantom consists of eight different materials varying in horizontal direction. The thickness of each material changes in vertical direction in three rows from 10 µm to 30 µm to 100 µm. In the lower area of the phantom, aluminum is applied in three different thicknesses to investigate the influence of beam hardening on material differentiation. The chosen thicknesses are 1 mm, 3 mm and 10 mm. The material thicknesses of the materials of interest behind the aluminum in the lower area of the phantom is constant with 30 µm at every layer of applied aluminum. In order to investigate the possibility of separating different medical contrast agents in one acquisition, iodine as well as gadolinium has been applied to the phantom. To create a solid iodine sample, an iodine based contrast agent [5] has been dissolved in water in different concentrations. Various filter papers were then soaked with these solutions. Once the water has vanished, the iodine has crystallized at the fibers of the filter paper, forming solid iodine samples in different relative thicknesses. The 10 µm

relative Gd sample has been created using the same method with an Gd-based contrast agent [6]. To investigate the limits of material separation, two elements with K-edges close to each other were attached, namely zirconium and niobium which K-edge energies varying by just 1 keV. Furthermore, polyethylene terephthalate (PET, $C_{10}H_8O_4$) was applied as control field as an absorbing material without K-edge in the investigated energy range. The absorption phantom was placed inside a 3D printed support structure for better handling. Figure 3 (left) shows a schematic drawing of the phantom, a photography of it is shown in the right part. The K-edge energies of the materials used are listed in table 1.

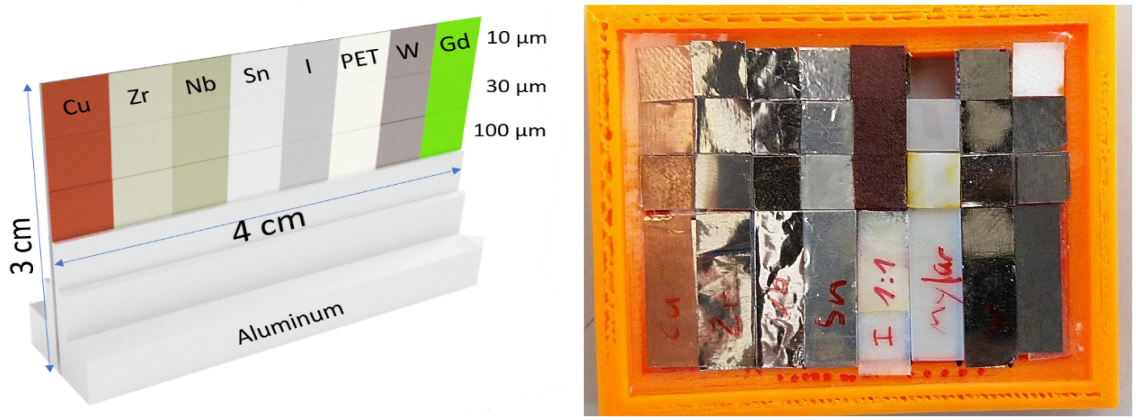

Figure 3. Structure of the absorption phantom. The materials are chosen in three different thicknesses varying in vertical direction. Left: schematic drawing of the phantom to illustrate the structure. Right: photography of the finished phantom without front layer of aluminum.

Table 1. Materials used in the phantom and corresponding K-edges (data from [2]).

Element	**Atomic Number / Z**	**K-edge [keV]**
aluminum	13	1.562
copper	29	8.993
zirconium	40	17.997
niobium	41	18.985
tin	50	29.211
iodine	53	33.168
gadolinium	64	50.207
tungsten	74	69.517
PET ($C_{10}H_8O_4$)	(6; 1; 8)	(0.283; 0.001; 0.532)

2.4 Experimental setup

For the spectroscopic X-ray imaging in this work, a micro CT setup was used. Inside a shielding box, an X-ray tube was installed as well as a movable detector holder with the Medipix3RX-detector and 1 mm CdTe sensor. The ability of precisely moving the detector allows to record objects

2020 JINST 15 P01006

larger than the active area of the sensor, by recording several tiles of the object and stitching these together afterwards. Between the detector and the X-ray tube the absorption phantom was placed. The distance from detector to X-ray tube was 56 cm, the distance from absorption phantom to detector was 11 cm. As a result, the phantom was recorded magnified 1.2 times. As X-ray source the Hamamatsu L10101 X-ray tube with tungsten target was used. It provides 5 kV–100 kV acceleration voltage with anode currents from 1 µA to 200 µA. The output window of the tube consists of 150 µm thick Beryllium.

The readout system is a combination of the FitPix [7] device for Medipix3RX and the Pixelman readout software [8], both developed by the Institute of Experimental and Applied Physics (IEAP) [9] to configure and readout the detector. Further information on the setup used can be found in [10].

2.5 Energy threshold calibration

In order to prepare the energy-selective radiographs, the differences of the energy thresholds per pixels were adjusted and an overall energy to threshold calibration was performed. To equalize the pixels, the noise floor method [8] was used. The Noise-Floor method is the fastest equalization tool but offers less accurate energy resolution than other equalization methods [11].

To determine the threshold-value to energy relation, known emission lines of radioactive sources and fluorescence photons from different elements were recorded over a certain range of energy. Therefore, the detector was placed outside the beamline recording mainly secondary photons emitted by the radiated materials caused by scatter and fluorescence processes. Every of the eight energy thresholds was shifted stepwise from low threshold values to higher threshold values while all events were recorded. The total events of all pixels per threshold were summed up to determine the total count rates of every threshold for every threshold value. By calculating the derivation of the total registered counts between each two threshold values, the measured X-ray spectrum could be determined. Figure 4 shows exemplarily a zirconium fluorescence measurement acquired with the first threshold (TH0) of the detector. The resulting X-ray spectrum with the fluorescence peak was fitted by a linear combination of a gaussian function and a straight line.

$$f(x) = \sqrt{\frac{\pi}{\omega \cdot 4 \cdot \ln(2)}} \cdot \exp\left(-4\ln(2) \cdot \frac{(x - x_0)^2}{\omega^2}\right) + bx + c$$

Here, b is the slope of the straight line, ω is the FWHM[1] of the Gaussian, x_0 is the center position of the Gaussian and A is the amplitude.

The center position of the gaussian function of each element were used as calibration values by comparing them to the recorded fluorescence energies. In total, the fluorescence peaks of six different materials were recorded by every energy threshold. Additionally, the strongest gamma photo peak of ^{152}Eu (121.78 keV) and ^{241}Am (59.54 keV) were used as calibration values. Because the limited energy resolution of the Medipix3RX detector, the detector was not capable of separating the K_a emission line from the K_β emission line. This led to a wider photo peak in the recording. In order to achieve a credible energy calibration, the center peak energies were weighted by multiplying the photoenergies with the transition probability of the involved energy levels. The weighted energy was then used as calibration value. In figure 5, the recorded center values of the fluorescence peaks

[1]Full Width Half Maximum.

2020 JINST 15 P01006

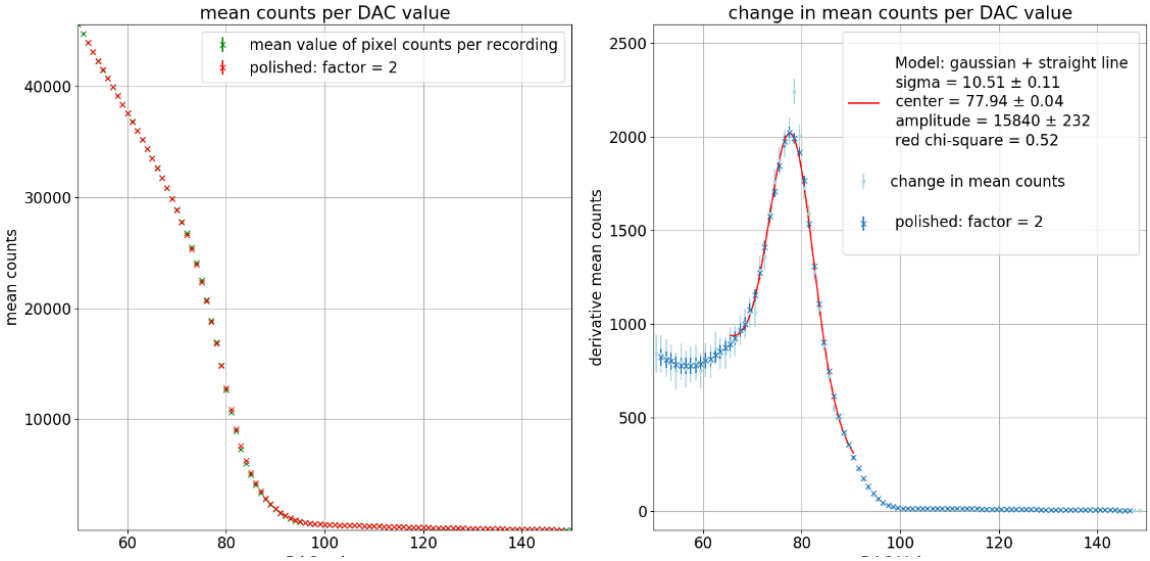

Figure 4. Exemplary fluorescence peak of zirconium recorded with MPX3RX threshold TH0. On the left side the total registered events per threshold is shown. On the right side the change of counts per energy is pictured.

are plotted exemplarily for threshold TH0 over the corresponding energy values. By fitting the data with a polynomial of second order, the relation between threshold value and corresponding energy could be described. The energy threshold relations of the other energy thresholds have similar shapes, which is why the representation of these has been omitted.

All measurements were performed in the super-high-gain mode of the Medipix3RX detector to enable the highest energy resolution. This gain mode determines the capacity of the feedback capacitors of the charge sensitive amplifier which is adjustable from 28 fF in the super-low-gain mode down to 7 fF in the super-high-gain mode [12]. The super-high-gain mode provides the best energy resolution but provides linearity only up to $5ke^-$ ($\approx$ 22 keV for CdTe) [1]. For higher energies the Charge Sensitive Amplifier (CSA) is not in the linear range anymore. This, led to the recorded parabolic energy-threshold relation exemplarily shown for threshold TH0 in figure 5.

2.6 Spectral image recording

The absorption phantom was acquired with an X-ray spectrum of 85 kVp maximum energy, shown in figure 6, 60 µA tube current and 1.25 times magnification. All threshold images were corrected with a flatfield image of the corresponding threshold to compensate sensor-related differences in pixel count rates. Defective pixels were corrected with a nearest neighbor interpolation. The phantom was recorded in three by four tiles merged afterwards into a total picture of the phantom. The flatfield image of threshold TH0 is exemplarily shown in figure 7 left, the corrected recording of TH0 is shown in figure 7 right.

The requirement for the recordings was to be at least 15000 recorded events in each pixel in each threshold in order to achieve credible statistics. In the single pixel spectral mode of the detector the counter depth of every single threshold is 12 Bit [1]. The counter values of each pair of thresholds are stored in a 32 Bit shift register, which allows to store both data packages in a single output number and, therefore, reduce the time used for the hardware-sided read out electronics. To reduce

2020 JINST 15 P01006

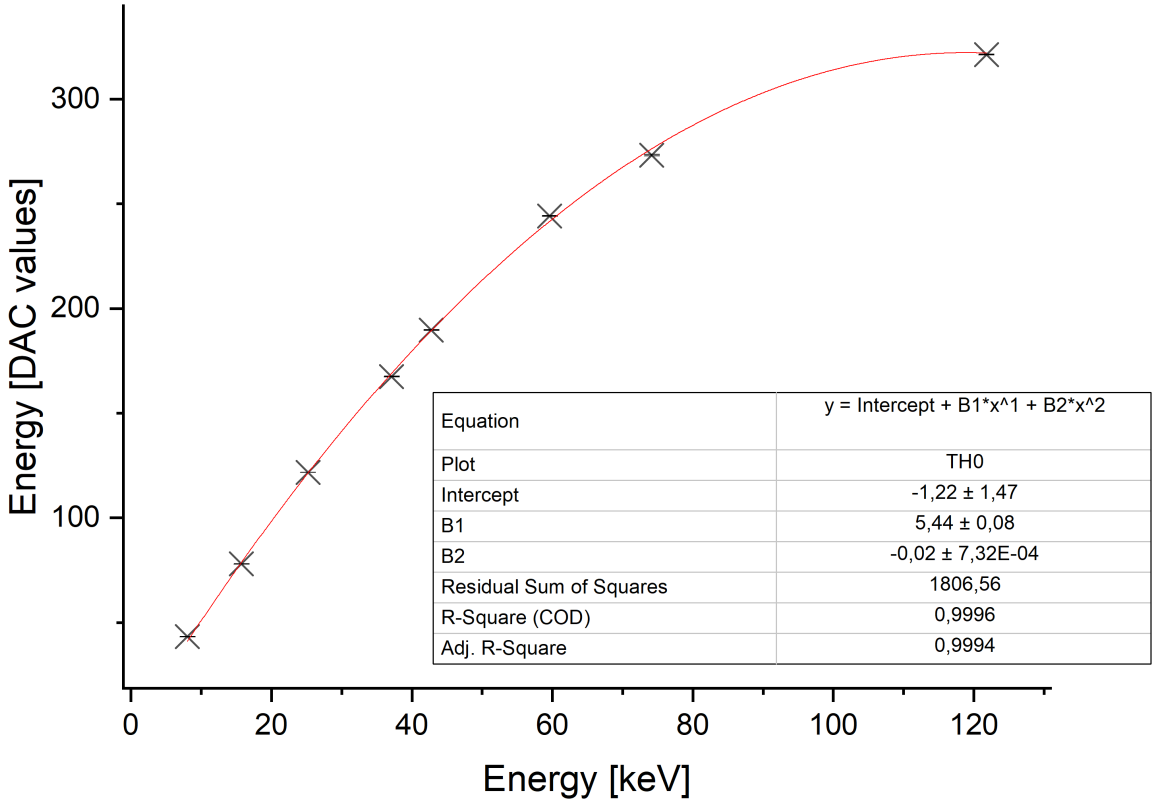

Figure 5. Energy threshold to energy relation exemplarily shown for threshold TH0. The recorded values of the fluorescence peaks are approximated with a second order polynomial to describe the energy threshold relation.

the number of files created, multiple recordings can be merged before the file is written. However, this can result in defective data files if the counters of the built-in images exceed 16 Bits. At this point, the shift register becomes overfilled and the data is corrupted. To prevent the shift-register from overflowing, the maximum number of summed images is limited to 16 Bits of counts per pixel and threshold. However, to achieve the required statistics, several integrated files must be written, the counter values separated afterwards and the counter values of the individual thresholds of each recording added subsequently. The final images were put together from 600 individual images per tile, each with a recording time of 1.125 s, resulting in a total measurement time of $(12 \cdot 600 \cdot 1.125)$ seconds for all 12 tiles, i.e. 135 minutes. The recording time of the Flatfield image was chosen to be the same. In addition to the shift register, the different counting rates of the energy thresholds caused difficulties. The energy threshold TH7 which is exclusively sensitive to the highest energetic photons of the incoming spectrum was set to the K-edge energy of tungsten at 69 keV. The recorded intensity of the counter of this threshold was very low compared to the intensity of the counter of the lowest energy threshold TH0 which was set to the K-edge energy of copper at 9 keV. As a result, the decreasing registered signal intensity at the threshold TH7 had to be statistically corrected. Furthermore, the intensity of an X-ray tube is not homogeneous over the whole energy range but a distribution dependent on the target material used (figure 6). The absorption probability of photons for every material with the sensor is varying relative to the incoming photon energy and the collected charge for an incident photon varies between the energy thresholds.

2020 JINST 15 P01006

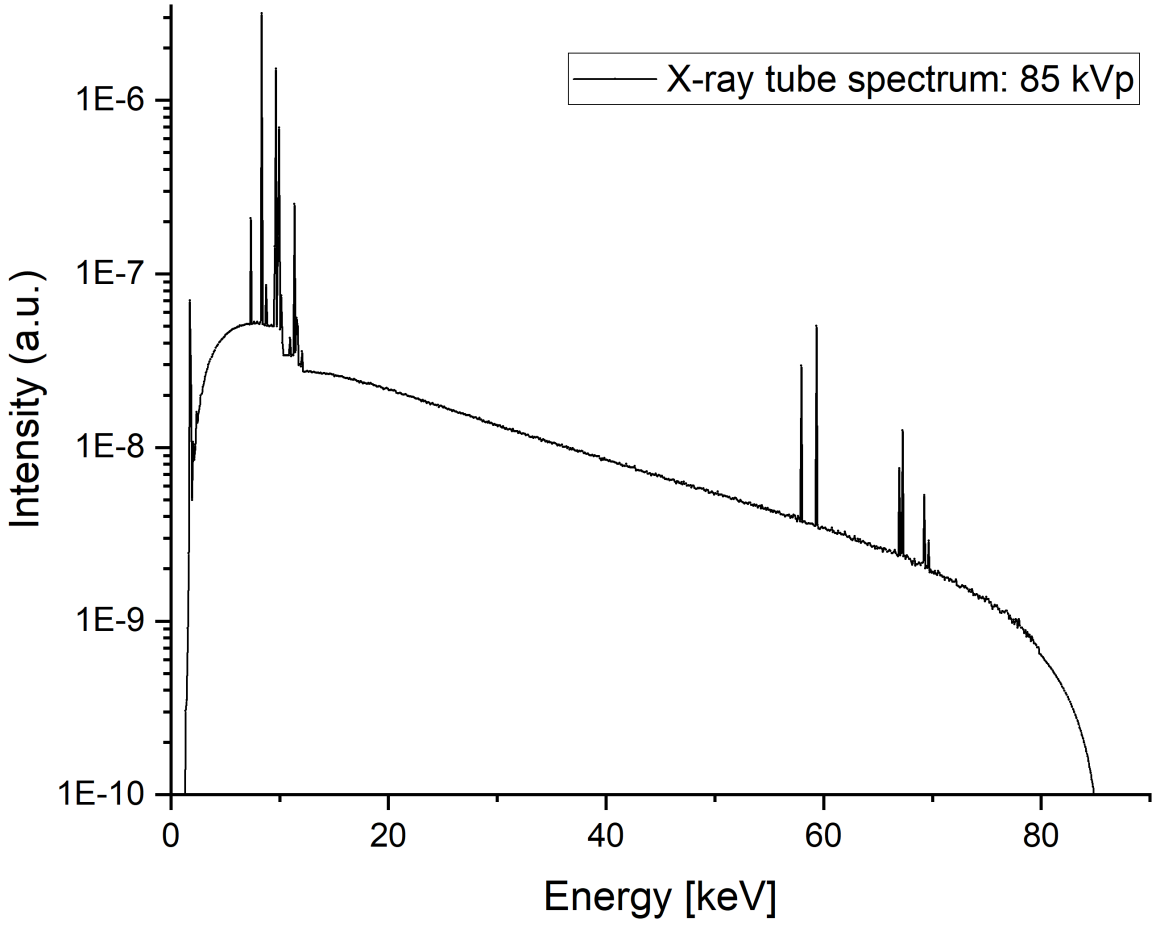

Figure 6. Simulated 85 kVp W-anode X-ray spectrum as used for recording of the phantom.

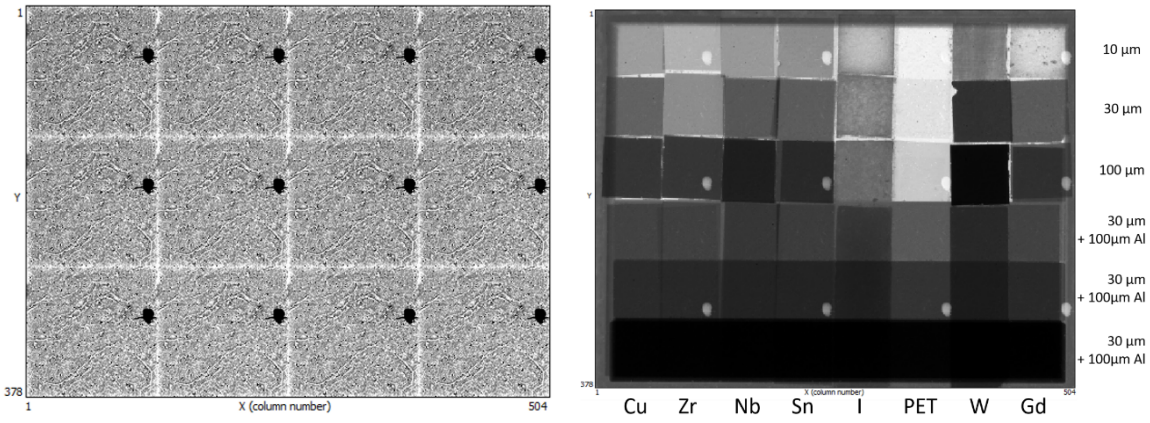

Figure 7. Left: image of the total flatfield recording of TH0. The image was created by joining 4×3 tiles together which can be seen from the dark spot caused by the connection of the high voltage to the sensor. Right: image of the total flatfield and nearest neighbor corrected phantom recorded at 85 kVp with TH0.

In order to consider the influencing factors on the counting rates of the individual threshold values, the 10 µm PET area of the absorption phantom was left empty to directly record the

2020 JINST 15 P01006

undisturbed X-ray spectrum. By normalizing the recordings on the registered counts in this empty area, all disturbing effects that influence the different count rates were taken into account. The raw images were later flatfield corrected and faulty pixels were corrected by a nearest neighbor interpolation to improve image quality.

2.7 Evaluation and material discrimination

The normalized and corrected images of the respective energy thresholds were subtracted from each other to create different energy windows ($W_{nm} = TH_n - TH_m | n < m$). It was always subtracted the higher energy threshold from the lower because the thresholds register all events above the thresholds. The resulting intensity of every pixel for every energy window was then compared between the energy windows. By a suitable subtraction of different energy windows $\mathrm{Res}_{nmij} = (W_{nm} - W_{ij} | n < m; i < j)$, it was possible to separate individual materials based on the intensities rate of change in the corresponding pixels.

Subtracting energy windows above the K-edge of a specific area (W_{ij}) from an energy window below the K-edge (W_{nm}) results in a higher intensity in the pixels of the resulting image (Res_{nmij}) where the K-edge is located between the energy windows. The pixels with the highest remaining count rates are the ones that had the greatest change in absorption and were separated from the others by comparing the count rates with a count rate threshold. This threshold was composed of a constant factor (a), the standard deviation of the count rate distribution of the entire resulting image (σ_{Res}) and the mean count rate of all pixels of the resulting image ($\mathrm{mean}_{\mathrm{Res}}$). All pixels with a resulting count value higher than the threshold $I_{\mathrm{min}} = \mathrm{mean}_{\mathrm{Res}} + a \cdot \sigma_{\mathrm{Res}}$ were assigned to the specific K-edge or material respectively in the corresponding energy window.

3 Results and discussion

By the comparison of various energy windows recorded in one measurement series, clear differences in the absorption of different material areas could be observed and several materials could be separated. The method described in section 2.7 was used to distinguish between the materials. The constant factor a was chosen as 1.5. The pixels with resulting count values above the threshold have been separated and colored for better viewing. The threshold values TH0 to TH7 were set on the K-edges of the materials starting with TH0 on the K-edge of copper (8.99 keV) to TH7 on the K-edge of tungsten (69.52 keV). The resulting pictures are shown in figure 8 to 11. By merging all colored images created this way, a total false color image of the phantom was created as shown in figure 11 on the right-hand side. All recordings were made in one measurement at 85 kVp.

The best result in terms of material discrimination was achieved for the separation of tungsten from the other materials as shown in figure 8 (right). Hereby, almost the whole column with all different material thicknesses could be revealed. gadolinium (figure 8 left) was also well distinguishable from the other materials. For iodine (figure 9 left) and tin (figure 9 right), the separation was not possible across the whole column and only the 100 µm areas and the 30 µm areas could be associated with the appropriate material.

A distinction between zirconium (figure 10 left) and niobium (figure 10 right) was not possible. The images of these two materials originating from the comparison of the energy windows had almost indistinguishable results, although the distinction between Zr and Nb and materials with

2020 JINST 15 P01006

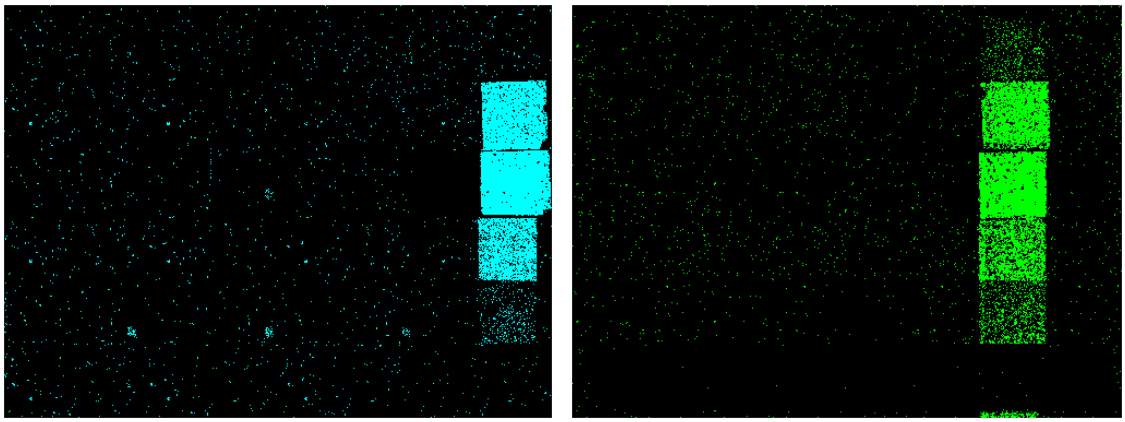

Figure 8. Left: false color image of pixels identified as gadolinium (W_{56}–W_{67}). Right: false color image of pixels identified as tungsten (W_{07}–W_{06}).

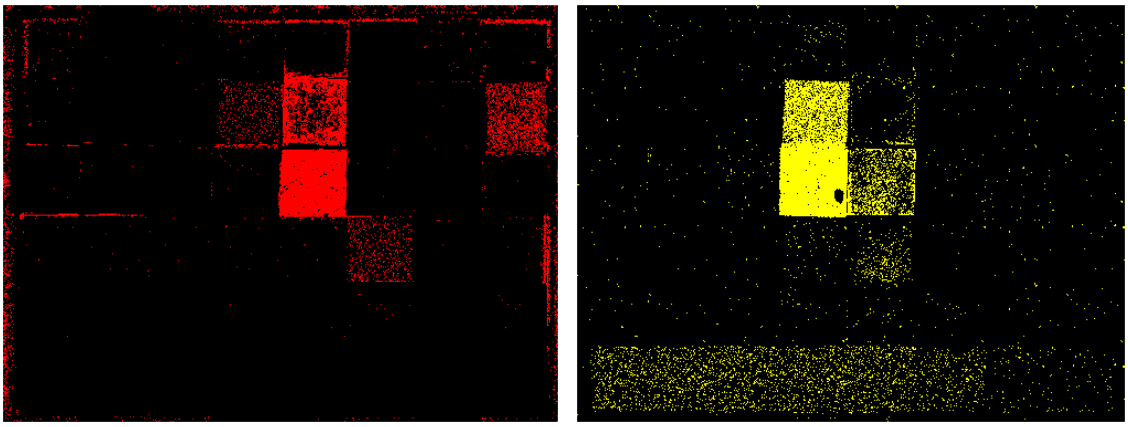

Figure 9. False color image of pixels identified as iodine (W_{24}–W_{03}). Right: false color image of pixels identified as tin (W_{34}–W_{46}).

higher atomic numbers was successful. The reason that niobium and zirconium could not be distinguished from each other was the limited energy resolution of the Medipix3RX because the K-edges of Zr and Nb are only 1 keV apart. The FWHM of the measured photopeak caused by the fluorescence calibration measurements was 2.5 keV at 18 keV. That means that the energy thresholds TH2 set at approximately 18 keV and TH3 set at approximately 19 keV did overlap and prevent a successful distinction of the materials.

Another reason why it was difficult to distinguish low atomic number elements and the areas with low thicknesses was the influence of low photo absorption in these areas on the recorded total spectrum.

The maximum energy of the X-ray spectrum used had to be above the K-edge of tungsten. This led to a very small signal change due to photo absorption in the low Z materials compared to the total spectrum which explains why copper (figure 11 left), niobium and zirconium could not be reliably distinguished. The absorption in any of the 10 µm thick areas was too small for a reliable material discrimination as well (cf. figure 11 right). Furthermore, the influence of the applied aluminum

2020 JINST 15 P01006

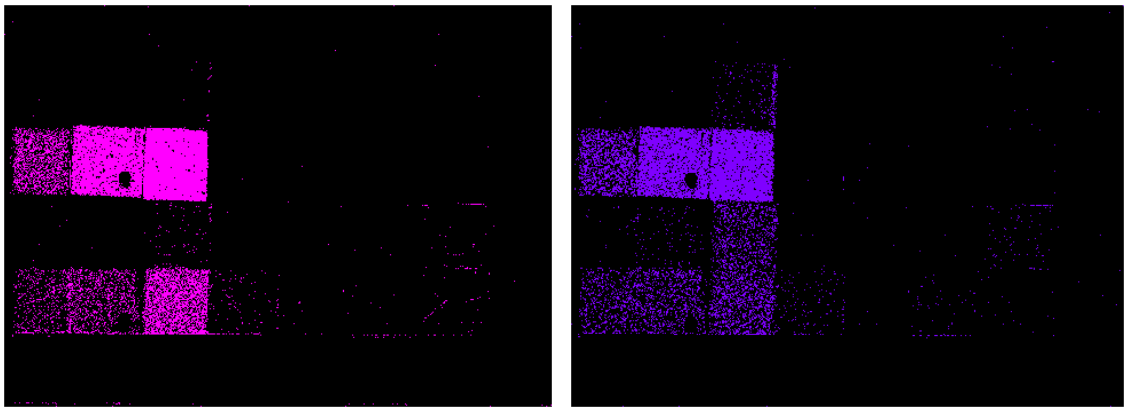

Figure 10. Left: false color image of pixels identified as niobium (W_{13}–W_{06}). Right: false color image of pixels identified as zirconium (W_{12}–W_{16}). Due to the limited energy resolution of the detector the materials are not distinguishable.

filter in the lower area of the phantom on the total spectrum was very high compared to the influence of the underlying 30 µm thick materials. Therefore, it was not possible to distinguish here materials other than tungsten for the used 85 kVp X-ray spectrum. For a discrimination of materials with low atomic numbers, the energy spectrum must be shifted to a lower maximum energy. This increases the influence of absorption on the total spectrum and therefore the SNR.

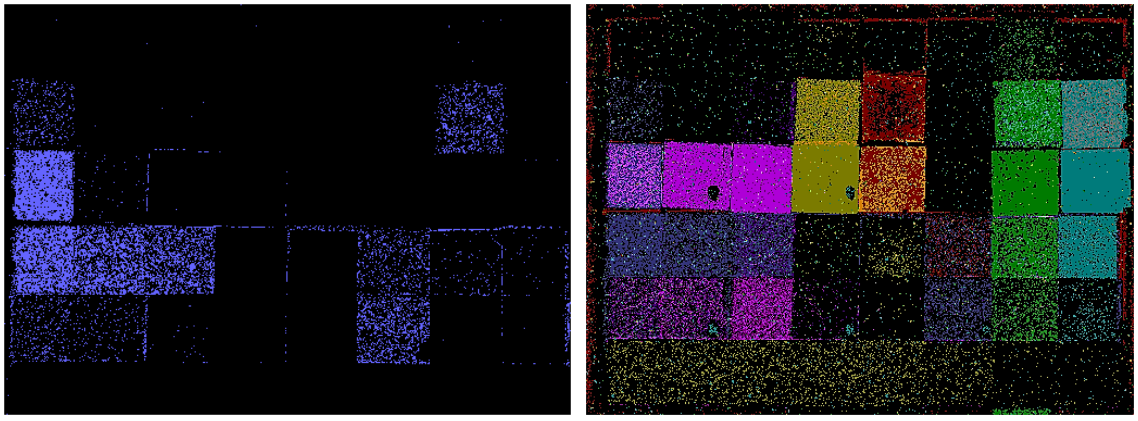

Figure 11. Left: false color image of identified copper pixels (W_{01}–W_{04}). Right: total false color image of all colorized pixels.

4 Conclusion

The Medipix3RX offers with its eight different energy thresholds the possibility of targeted and rapid material differentiation and even material identification in one single X-ray image by K-edge method. By comparing the photo absorption of the materials in different energy ranges, it was possible to separate different materials and assign them to a specific element. With the X-ray tube spectrum created with 85 kVp maximum energy, the elements with a high Z-number, i.e. tungsten

2020 JINST 15 P01006

and gadolinium, could be clearly separated from the other materials. Tin and iodine could be distinguished from the other materials in the area of the highest material thickness and gadolinium and iodine could be distinguished reliably from each other. A material differentiation of zirconium and niobium was not possible here due to the limited energy resolution of the detector and the used high-kVp X-ray spectrum. For the same reason a material distinction of copper as well as the areas of lowest material thickness could not be achieved. To distinguish elements with low atomic numbers, the energy spectrum must be adjusted to lower energies.

In conclusion, it can be said that a material differentiation by the K-edge method with the Medipix3RX is highly applicable under proper conditions. It must be ensured that the K-edges of the elements are further apart energetically than the maximum energy resolution of the detector in the specific energy range and the absorption by the materials must have enough influence on the incident X-ray spectrum. In order to improve these results in future investigations, an improvement of the threshold equalization is planned. This will be based on a monochromatic radiation source. In addition, an object recognition algorithm will be implemented, and it will be examined whether the result of material recognition can be further improved in comparison to pixel wise differentiation. The object-based recognition may reduce falsification of the material recognition by noise. Furthermore, the possibility of material identification will be investigated under direct consideration of the energy-dependent absorption coefficients as an alternative approach of material identification.

To make material differentiation practicable for most applications like medical imaging with multiple contrast agents or material identification in non-destructive analysis (NDA), the active area of the detector must be increased. This can be achieved by tiling several Medipix3RX detectors next to each other to one large detector using edge-less sensors as shown by Jakubek et al. [13]. By use of this tiling technique, a $14 \times 14\,\mathrm{cm}^2$ detector was realized. In [13] Timepix chips have been used, but the same way large area Medipix3RX based detectors can be built. As there is no limit in scale-up of this method, this way large area detectors with $24 \times 30\,\mathrm{cm}^2$ can be set up as demanded by mammography, medical imaging of extremities and NDA. For computed tomography (CT) usually row detectors are used with a size of $3 \times 45\,\mathrm{cm}^2$. Such row detectors can be built with Medipix3RX chips as well. Due to the small pixel size of Medipix3RX detectors, the maximum flux without pile-up is $3 \cdot 10^8$ photons/mm^2/s. As the flux in a CT system is up to 10^9 photons/mm^2/s, an improvement of the Medipix3RX is necessary for its use in current CT systems.

Acknowledgments

The authors would like to thank G. Blaj for simulation of the X-ray spectra.

References

[1] R. Ballabriga et al., *The Medipix3RX: A high resolution, zero dead-time pixel detector readout chip allowing spectroscopic imaging*, 2013 *JINST* **8** C02016.

[2] J.H. Hubbell and S.M. Seltzer, *X-Ray Mass Attenuation Coefficients*, NISTIR 5632 (2004) [https://doi.org/10.18434/T4D01F].

2020 JINST 15 P01006

[3] M.J. Berger et al., *XCOM: Photon Cross Sections Database*, NBSIR 87-3597 (2010) [https://doi.org/10.18434/T48G6X].

[4] CERN, *Medipix3 collaboration*, (2019) https://medipix.web.cern.ch/collaboration/medipix3-collaboration.

[5] Gelbe Liste Online, *Imeron® 400 MCT, 400 mg Iod/ml, Injektionslösung, Infusionslösung,* 500 *ml*, (2019) https://www.gelbe-liste.de/produkte/Imeron-400-MCT-400-mg-Iod-ml-Injektionsloesung-Infusionsloesung-500-ml_499239.

[6] Gelbe Liste Online, *Fachinformation: ProHance®,* 0, 5 *M, Injektionslösung* 10 *ml*, (2019) https://www.gelbe-liste.de/produkte/ProHance-0-5-M-Injektionsloesung-10-ml_526478/fachinformation.

[7] V. Kraus, M. Holik, J. Jakubek, M. Kroupa, P. Soukup and Z. Vykydal, *FITPix: Fast interface for Timepix pixel detectors*, 2011 *JINST* **6** C01079.

[8] D. Turecek, T. Holy, J. Jakubek, S. Pospisil and Z. Vykydal, *Pixelman: a multi-platform data acquisition and processing software package for Medipix2, Timepix and Medipix3 detectors*, 2011 *JINST* **6** C01046.

[9] Czech technical university in Prague, *Institute of Experimental and Applied Physics*, (2019) https://www.cvut.cz/en/institute-of-experimental-and-applied-physics.

[10] S. Procz et al., *Medipix3 CT for material sciences*, 2013 *JINST* **8** C01025.

[11] S. Procz, J. Lubke, A. Zwerger, M. Mix and M. Fiederle, *Optimization of Medipix-2 Threshold Masks for Spectroscopic X-Ray Imaging*, *IEEE Trans. Nucl. Sci.* **56** (2009) 1795.

[12] R. Ballabriga and X. Llopart, *Medipix3RX manual*, CERN (2012).

[13] J. Jakubek et al., *Large area pixel detector WIDEPIX with full area sensitivity composed of 100 Timepix assemblies with edgeless sensors*, 2014 *JINST* **9** C04018.

2020 JINST 15 P01006